Automated Slice-Based Artery Identification in Various Field-of-View CTA Scans

D. Major, A. A. Novikov, M. Wimmer, J. Hladůvka, and K. Bühler

VRVis Center for Virtual Reality and Visualization, Vienna, Austria

Abstract

Automated identification of main arteries in Computed Tomography Angiography (CTA) scans plays a key role in the initialization of vessel tracking algorithms. Automated vessel tracking tools support physicians in vessel analysis and make their workflow time-efficient. We present a fully-automated framework for identification of five main arteries of three different body regions in various field-of-view CTA scans. Our method detects the two common iliac arteries, the aorta and the two common carotid arteries and delivers seed positions in them. After the field-of-view of a CTA scan is identified, artery candidate positions are regressed slice-wise and the best candidates are selected by Naive Bayes classification. Final artery seed positions are detected by picking the most optimal path over the artery classification results from slice to slice. Our method was evaluated on 20 CTA scans with various field-of-views. The high detection performance on different arteries shows its generality and future applicability for automated vessel analysis systems.

Categories and Subject Descriptors (according to ACM CCS): I.4.8 [Image Processing and Computer Vision]: Scene Analysis—Object recognition

1. Introduction

Centerline extraction, labeling and segmentation of arteries in CTA scans play a key role in clinical vessel analysis. They are used to detect and quantify arterial diseases such as stenosis and aneurysms, and therefore support physicians in making a diagnosis. Carotid arteries and peripheral arteries are well-known regions of occurrence of such diseases [LAU*06,FHR06]. In order to start the vessel analysis in a CTA scan physicians have to locate the artery of interest first (e.g., the left common carotid artery), mark its centerline and segment its lumen which is a highly time consuming procedure. For that reason, many recent works targeted this problem and developed vessel analysis systems which assist physicians by automated centerline tracking, lumen segmentation [GYD*14, LL] and disease quantification [TvWH*13]. However, the aforementioned systems require user interaction for setting an initial position into a specific artery and its anatomical label. This information is necessary to start tracking the artery tree, label it anatomically and map the disease quantification results to the corresponding arteries. Automating the manual user interaction step would optimize the clinical workflow even more. Physi-

cians would only need to review, and if necessary adjust the automatically produced results before they make a diagnosis. We present a fully automated framework to identify and anatomically label five different main arteries from three parts of the human body and place seed positions in each of them. The detected seed positions and the label of an identified artery serve as an automatic initialization of vessel analysis systems. The five arteries we target are the two common iliac arteries in the pelvis, the descending aorta in the abdomen and chest, and the two common carotid arteries in the neck. Our approach recognizes first the field-of-view of the scan and proceeds with the detection of arteries present in the scanned body region. For each selected artery the centerline positions are regressed using Nearest Neighbor regression on slices where it is present. The regression result is then refined by classifying the regressed positions using a Naive Bayes classifier. For the classification we introduce an anatomical feature which captures the distance between the arteries and the spine. The slice-wise artery classification results are finally transformed to costs and the positions selected by a minimum cost path algorithm correspond to seed positions within the artery of interest.
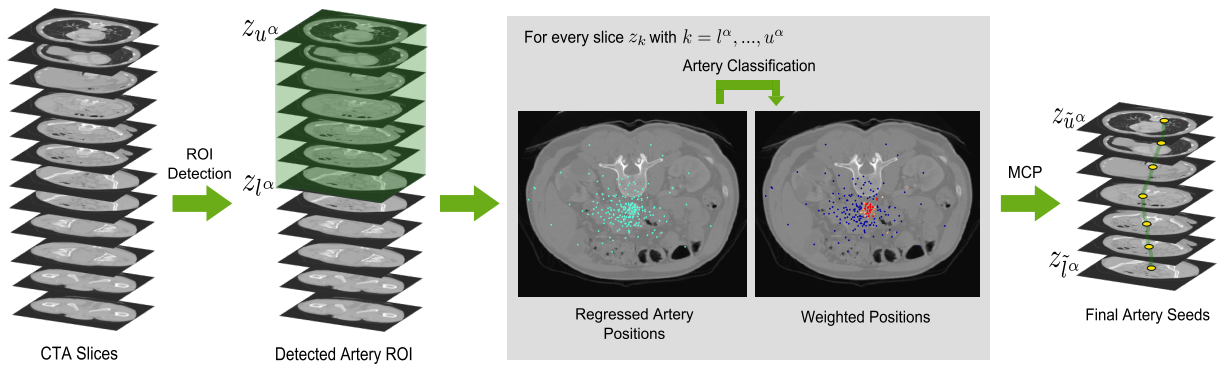
Figure 1: *Overview of the artery identification framework: The ROI is depicted as a transparent green box, the regressed artery position candidates are visualized in aquamarine. After classification, the positions are shown in red in case of a highly probable artery candidate and in blue in case of a highly probable non-artery candidate. The final artery seeds are yellow dots.*

Several recent works aimed to find arteries automatically in CTA or CT data. They can be categorized into approaches which localize solely arteries as it is done in this work and into methods which detect bifurcations and connected arteries. Sanderse et al. [SMH*05] targeted the detection of carotid arteries in CTA scans covering head and neck. First, a shoulder landmark is detected and carotid arteries are then extracted in a slice-wise manner by Circular Hough Transform. Final artery landmarks are detected using a 3D hierarchical clustering approach. The algorithm was evaluated on 31 datasets and a detection rate of 88% was reported. Zheng et al. [ZCG14] introduced an automatic aorta detection and tracking approach in non-contrast cardiac CT scans. First, slice images containing the heart are selected based on average intensities. As a next step, Generalized Hough Transform is applied to find the aorta slice-wise and a 3D k-means clustering approach helps to find the final seed positions for the ascending and descending aorta. The whole aorta was successfully tracked from the seed positions using a Bayesian framework in 24 CT scans. Both aforementioned algorithms are designed to detect specific arteries coming from a specific body region and their general application to different artery types is consequently hard or impossible. The framework of Beck et al. [BBBD10] detects carotid bifurcations with the surrounding arteries. The bifurcation Region of Interest (ROI) is localized using a machine learning approach similarly to our method. Fast Marching is applied to segment the arteries of interest. The segmentation skeletons are finally compared to a previously created knowledge base in order to identify a bifurcation of interest. The carotid bifurcations were detected in 50 CTA scans with 74.47% success rate for the left part and 78.72% for the right part. The algorithm of Brozio et al. [BGG*12] detects the iliac bifurcations and connected arteries. First, the ROI is detected similarly to Beck et al. [BBBD10] followed by a slice-wise artery candidate detection using thresholding. Connected Component Analysis and size prefiltering is per-

formed as a next step slice by slice. The candidates are then connected to a squared distance graph which is traversed by the Dijkstra algorithm to get the artery candidates. Finally, the best candidates are chosen considering an additional set of features. The method was tested on 119 datasets where the iliac bifurcation was labeled in 75.63% of the cases correctly and the common iliac and one of its branches were detected in 82.77% of the cases correctly. The previous two works presented detection results of specific bifurcations, but the authors claim that their method is applicable to other bifurcations as well. However, modeling different types of bifurcations is more complex than modeling single arteries. In this work we introduce a chain of machine learning techniques with a simple set of features which is general enough to successfully identify different kinds of single arteries.

Our main contributions are two-fold. First, we apply a novel chain of machine learning techniques including a new anatomical feature to identify specific arteries. Second, we present results on five different arteries from three body regions in scans with varying field-of-views, which proves the robustness and generality of our method.

The rest of this paper is organized as follows: The steps of our algorithm are described in Section 2 and evaluated in Section 3. Our conclusion and future work are in Section 4.

2. Methods

Our artery identification framework detects five different arteries: The left common iliac (LCI) and the right common iliac (RCI) in the pelvis, the descending aorta (AO) in the abdomen and chest, and the left common carotid (LCC) and the right common carotid (RCC) arteries in the neck, denoted in the following by α, where $\alpha \in \{LCI, RCI, AO, LCC, RCC\}$. The input to our algorithm is a CTA scan $\mathcal{V} = \{z_j\}, j = 1,...,n$ given as an ordered set of n slices. All CTA scans have a feet-to-head

face-up orientation and intensities in Hounsfield Units (HU) (see Section 3.1). The task is then to return a set of artery seed positions $\{\mathbf{s}^\alpha_{z_i}\}, i = \tilde{l}^\alpha, ..., \tilde{u}^\alpha$ for every present artery of interest α in the region $\tilde{\mathcal{R}}^\alpha = \{z_i\}, i = \tilde{l}^\alpha, ..., \tilde{u}^\alpha, \tilde{\mathcal{R}}^\alpha \subseteq \mathcal{V}$ with slice lower bound $\tilde{l}^\alpha$ and upper bound $\tilde{u}^\alpha$ where α was localized. Our method starts with ROI detection and delivers a region $\mathcal{R}^\alpha = \{z_k\}, k = l^\alpha, ..., u^\alpha, \mathcal{R}^\alpha \subseteq \mathcal{V}$ for each α. Possible artery candidate positions are regressed on every detected slice in $\mathcal{R}^\alpha$. The candidate positions are then classified into artery or non-artery classes. The ROI is refined to $\tilde{\mathcal{R}}^\alpha = \{z_i\}, i = \tilde{l}^\alpha, ..., \tilde{u}^\alpha, \tilde{\mathcal{R}}^\alpha \subseteq \mathcal{R}^\alpha$ based on the classification result and the classification probabilities are finally used to detect each $\mathbf{s}^\alpha_{z_i}$ using the Minimum Cost Path (MCP) algorithm. Figure 1 gives an overview of the framework, each step is described in this section in detail.

2.1. ROI Detection

After loading slices of a CTA scan, the first step is to localize the slices which contain the arteries α present in the scan. We apply machine learning in this step. For training data generation, we first map the slice numbers $j \in \mathbb{N}$ of $z_j \in \mathcal{V}$ to a global standardized body height space $h : \mathbb{N} \rightarrow [0, 1] \subset \mathbb{R}$, based on manually set landmarks where $h(j) = 0$ corresponds to the toes and $h(j) = 1$ to the top of the head. This step gives information about the field-of-view of the scan. To be able to decide if a field-of-view contains an artery ROI, we capture the body height intervals covering the arteries in the global standardized body height space. We use for this purpose ground-truth annotations of transformed slice lower $h(l^\alpha)$ and upper bounds $h(u^\alpha)$ in the data for each artery.

To be able to transform slice numbers to global standardized body height space values in unseen data, we apply the method of Graf et al. [GKS*11]. The authors compute image descriptors of bone and soft tissues on every slice. The mapping $h(.)$ is finally learned by Nearest Neighbor regression using the slice descriptors and the global standardized body height values of the training data. In order to localize ROIs of arteries α in unseen data we use the method of Cavallaro et al. [CGK*11]. Given a learned mapping $h(.)$, a ROI query is performed in an unseen scan by selecting initial candidates $h(j)$ which match $h(l^\alpha)$ and $h(u^\alpha)$ with an initial error e. It is continued with an iterative search for candidates with smaller errors than e using an interpolation and regression combination. The method finally delivers slice lower and upper bounds l^α and u^α, and determines the ROI $\mathcal{R}^\alpha = \{z_k\}, k = l^\alpha, ..., u^\alpha$ for every present artery.

2.2. Slice-wise Regression of Artery Positions

After a ROI $\mathcal{R}^\alpha$ covering an artery of interest α is detected, candidates for the artery slice-positions $\{\mathbf{a}^\alpha_{z_k}\}, k = l^\alpha, ..., u^\alpha$ are localized slice-wise. Artery slice-positions are derived from centerline annotations of medical experts (see later in Section 3.1).

First, the body boundary is detected on a slice z_k by applying the contour tracing algorithm proposed by Graf et al. [GKS*11] on pixels with intensities greater than -500 HU. This step helps us to concentrate solely on the body region of a slice. Afterwards, M slice-positions $\{\mathbf{r}^m_{z_k}\}, m = 1, ..., M$ are sampled via Gaussian sampling from the center of the detected body boundary. As a next step, we extract features around every sampled position. We compute Histogram of Oriented Gradients (HOG) [DT05] feature vectors in 80×80 mm image patches around each position. We chose the HOG features due to their excellent performance on medical images demonstrated in recent works [EGK*10, LKZ14]. After features are extracted on a slice z_k, the candidate positions $\{\hat{\mathbf{a}}^m_{z_k}\}, m = 1, ..., M$ for $\mathbf{a}^\alpha_{z_k}$ are extracted based on a previously trained machine learning model. We use a regression based technique for this task where we capture the relationship between the feature vectors and displacement vectors from each $\mathbf{r}^m_{z_k}$ to $\mathbf{a}^\alpha_{z_k}$ using training data. Emrich et al. [EGK*10] introduced an effective and simple regression technique called Instance-based Nearest Neighbor regression. It performs Nearest Neighbor search in a two-stage manner. First, κ_1 nearest neighbor samples are collected from each instance in a training set where they refer to a CT scan as an instance. Once they are collected, the κ_2 nearest neighbors are taken out of the κ_1-collection and regression is performed on them. We apply the aforementioned method with the extension that we take the κ_1 nearest neighbors only from those CTA scan instances which have the same value in the global standardized body height space as $h(k)$ of a query slice z_k. To account for the error of the mapping $h(.)$, we subdivided each training scan into overlapping consecutive sets of slices instead of single slices and test whether $h(k)$ falls into a region or not. To accelerate the Nearest Neighbor search in our high dimensional HOG feature space we apply the Priority Search K-Means Tree (K-Means Tree) algorithm presented recently by Muja et al. [ML14].

2.3. Slice-wise Candidate Classification

The artery position regression delivers M possible candidate positions per artery α slice-wise. The task is to find the candidates on each slice in $\mathcal{R}^\alpha$ which hit the artery of interest. Therefore, we first segment the underlying structure locally around each candidate $\hat{\mathbf{a}}^m_{z_k}$ on a slice z_k. We consider 60×60 mm regions around the points for the segmentation which is big enough to accommodate any artery of interest. Neila et al. [MNBA14] recently proposed a fast and powerful approximation method to optimize the functional of Active Contours Without Edges. We apply their method for segmentation of the underlying structures. If a segmentation Q is round, has an average intensity similar to injected contrast media and has a specific location we assume that it is a cross-section of an artery of interest. For that reason, we
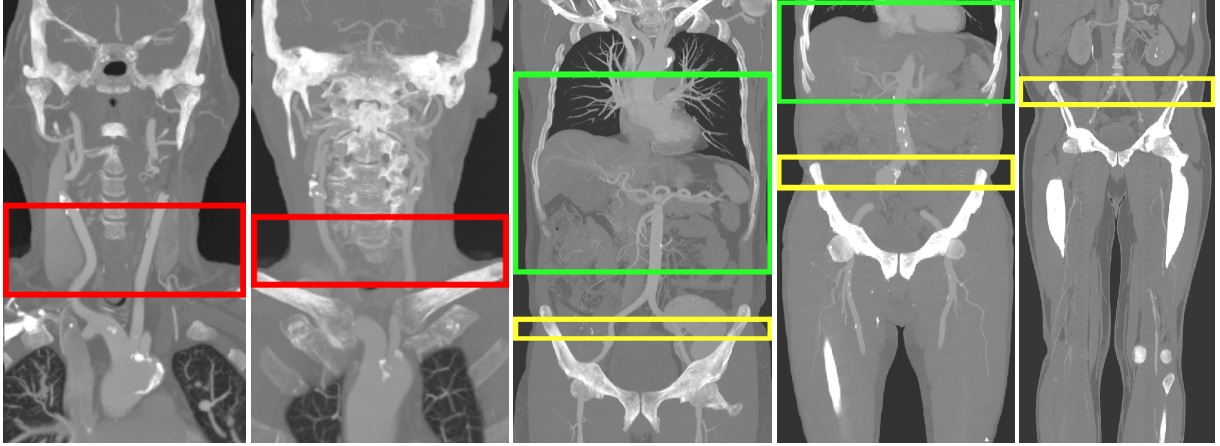
Figure 2: *Maximum intensity projection images of ROI detection results. Red rectangles mark the LCC and RCC slices, green rectangles the AO slices and yellow rectangles the LCI and RCI slices.*

model roundness (x_1) and average intensity (x_2) as follows:

$$x_1 = (4\pi A)/\ell^2, \qquad (1)$$

$$x_2 = \frac{1}{|Q|} \sum_{\mathbf{q} \in Q} I_{\mathbf{q}}. \qquad (2)$$

A corresponds to the area of the segmentation and ℓ to the length of the contour of the segmentation in Equation 1, and $I_{\mathbf{q}}$ is the intensity at a position $\mathbf{q}$ of the segmentation Q in Equation 2. All our arteries of interest are located next to the spine. For that reason we model their anatomical relationship as a feature. Hladůvka et al. [HMB15] presented an easy-to-use and robust method for detecting the center of the spinal canal in CT scan slices covering the spine. We apply their method to detect the spinal canal center $\mathbf{c}_{z_k}$ per slice. X- and y-displacements from $\mathbf{c}_{z_k}$ to each vessel candidate position $\hat{\mathbf{a}}_{z_k}^m$ are then computed (see Equations 3 and 4).

$$x_3 = c_{z_k}^x - \hat{a}_{z_k}^{m,x} \qquad (3)$$

$$x_4 = c_{z_k}^y - \hat{a}_{z_k}^{m,y} \qquad (4)$$

The aforementioned features represent our feature vector $\mathbf{x} = (x_1, ..., x_4)$ for classification into an artery of interest C_1 or not C_2. The classification models are trained on ground-truth segmentations around artery slice-positions and arbitrary positions sampled outside the ground-truth segmentations in the training data. The classification into the two classes C_1 or C_2 is performed by a Naive Bayes classifier (see Equations 5 and 6).

$$P(C_v|\mathbf{x}) = P(C_v) \prod_{b=1}^{4} P(x_b|C_v) \qquad (5)$$

$$\hat{v} = \underset{v \in \{1,2\}}{\arg\max} \, P(C_v|\mathbf{x}) \qquad (6)$$

2.4. Extraction of Artery Seeds

After classifying each candidate $\hat{\mathbf{a}}_{z_k}^m$ into C_1 or C_2, we start with a slice selection procedure in order to make sure that the artery of interest is present. Therefore, we iterate through the slices from l^α to u^α. We stop at the first slice which contains at least one candidate classified into C_1 and save its position into $\tilde{l}^\alpha$. We do the same starting from u^α towards l^α and save the position of the first slice into $\tilde{u}^\alpha$. If the condition $\tilde{l}^\alpha < \tilde{u}^\alpha$ holds, $\tilde{l}^\alpha$ and $\tilde{u}^\alpha$ are our final slice lower and upper bounds which determine our refined ROI $\tilde{\mathcal{R}}^\alpha = \{z_i\}, i = \tilde{l}^\alpha, ..., \tilde{u}^\alpha$. As a next step we iterate through all slices of $\tilde{\mathcal{R}}^\alpha$ and extract the best candidate on every slice based on classification posterior probabilities $P(C_1|\mathbf{x})$ and $P(C_2|\mathbf{x})$. A selection of candidates with maximum $P(C_1|\mathbf{x})$ from slice to slice is a possible but not robust way due to intermediate slices with maximum probabilities at outlier positions. Therefore, we use an MCP search algorithm which selects a minimum cost path over slices considering one candidate per slice. The MCP includes basic geometric constraints in order to avoid big jumps from one slice to an other due to outliers. The costs c for the MCP are defined as the transformed odds ratio (OR) by Yule's coefficient of colligation [Yul12, BFH07]:

$$c = \frac{\sqrt{OR} - 1}{\sqrt{OR} + 1} \text{ with } OR = \frac{P(C_2|\mathbf{x})/(1 - P(C_2|\mathbf{x}))}{P(C_1|\mathbf{x})/(1 - P(C_1|\mathbf{x}))}. \qquad (7)$$

The candidates selected by the MCP algorithm are the seed positions $\{\mathbf{s}_{z_i}^\alpha\}, i = \tilde{l}^\alpha, ..., \tilde{u}^\alpha$ per artery which is the final output of our framework.

	l-deviation [mm]	u-deviation [mm]	Overlap
LCI RCI	14.66 ± 10.78	15.72 ± 12.20	52.1 %
AO	22.55 ± 22.73	13.44 ± 10.07	86.9 %
LCC RCC	10.20 ± 5.51	9.45 ± 4.69	68.8 %
All	16.87 ± 17.31	12.81 ± 9.75	72.8 %

Table 1: *ROI detection results: Lower/upper bound deviation statistics from ground-truth and average overlap.*

	SRE [mm]	MCPE [mm]	AIDR
LCI	17.80 ± 5.06	4.45 ± 2.83	100 %
RCI	14.44 ± 10.54	5.85 ± 5.47	98.3 %
AO	14.73 ± 7.41	8.70 ± 3.15	98.3 %
LCC	13.55 ± 5.15	2.80 ± 1.79	93.4 %
RCC	12.31 ± 5.13	4.76 ± 3.90	71.5 %
All	14.66 ± 7.26	6.52 ± 4.13	94.4 %

Table 2: *Slice-based artery seed detection results (SRE = Slice regression error, MCPE = MCP error, AIDR = Artery identification rate).*

3. Evaluation

In this section we show leave-one-out cross-validation results of our artery identification framework on 20 CTA scans. First, we describe the CTA data, then we show intermediate and final evaluation results.

3.1. Datasets

Our data contains 20 diversely cropped contrast-enhanced CTA scans from three different vendors including 5 instances with legs, 9 scans with torso and 6 scans with neck. The CTA scans have feet-to-head face-up orientation and contain intensities in HU. The leg scans contain artery centerline annotations for *LCI* and *RCI*, the torso scans contain *AO* centerline annotations and the neck datasets include annotations of *LCC* and *RCC* arteries. Ground-truth centerline positions have been annotated in 3D by a medical expert. Each artery slice-position $\mathbf{a}_{z_k}^{\alpha}$ was finally generated through linear interpolation of the ground-truth positions. Ground-truth segmentations for all arteries were generated additionally on each slice. The pixel sizes of the 512×512 axial images range from 0.32 mm to 0.96 mm, and the slice distances vary from 0.3 mm to 1.5 mm. The smallest and largest scan comprise of 277 and 1743 slices respectively. All slice images were resampled to 1×1 mm. For the leg scans we sampled slices every 1 mm, for the torso scans every 4 mm and for the neck scans a slice spacing of 2 mm was used.

3.2. ROI Detection Performance

In order to measure how well the artery slices were detected we performed leave-one-out cross-validation with all 20 CTA scans. First, we measured the performance of the learned mapping $h(.)$ to the global standardized body height space. The overall average error was 28.15 ± 45.28 mm for slices where arteries α were present in all 20 CTA scans. Second, the performance of the ROI detectors was evaluated. The arteries *LCI*, *RCI* and *LCC*, *RCC* had nearly the same $h(l^{\alpha})$ and $h(u^{\alpha})$ in all our scans, thus we detected only *LCI* and *LCC* and assigned the detected regions also to *RCI* and *RCC*. The ROI detection step returned for each left-out scan l^{α} and u^{α} for the arteries present in the scan. After rejecting detections with missing lower and/or upper bounds

and checking if $l^{\alpha} < u^{\alpha}$ and $h(l^{\alpha}) < h(u^{\alpha})$ holds we got valid region detections for completely present arteries in all 20 scans. Furthermore, we evaluated the overlap between the slices with artery ground-truth and our detections. The average slice overlap for all artery ROI detectors was 72.8% with average distances to ground-truth of 16.87 ± 17.31 mm for the lower bounds and 12.81 ± 9.75 mm for the upper bounds. The ROI detection results are shown in Figure 2 and summarized in Table 1. We reached the highest overlaps with ground-truth in the *AO* region, followed by *LCC*, *RCC* and *LCI*, *RCI*. The low overlaps were due to ROI detections which were subsets of the ground-truth regions. This is more preferable than shifted detections outside of the ground-truth.

3.3. Slice-wise Artery Regression Performance

We measured the regression performance by computing the distance between $\mathbf{a}_{z_k}^{\alpha}$ and the mean of the M regressed candidate positions $\{\hat{\mathbf{a}}_{z_k}^{m}\}$ on each slice of $\mathcal{R}^{\alpha}$ and refer to it as slice regression error (SRE). We sampled $M = 500$ positions on each slice via Gaussian sampling. The instance based regression parameters κ_1 and κ_2 were set to $\kappa_1 = 1$ and $\kappa_2 = 3$ as proposed by Graf et al. [GKS*11]. Altering these values had no significant influence on the results. The K-Means Tree showed the best performance with a branching factor of 128 and number of iterations of 15, which have been proposed by Muja et al. [ML14]. For extraction of the HOG feature vectors the method of Dalal et al. [DT05] was used where 324-dimensional feature vectors were extracted with 9 orientation bins and 4×4 cells for each 80×80 mm patch. Leave-one-out cross-validation runs were set up among CTA scans containing the same artery region, thus we took the 139 artery slices from the 5 leg scans to cross-validate the artery position regression for the *LCI* arteries, the 483 artery slices from the 9 torso scans to cross-validate the regression for *AO* positions, etc. In each run the artery slices of a scan were selected for testing and all artery slices of the remaining scans were used for training. The overall average distance to ground-truth was 14.66 ± 7.26 mm considering all cross-validation runs. The cross-validation performances per artery are summarized in Table 2.

(a)　　　　　　　　　　　(b)　　　　　　　　　　　(c)
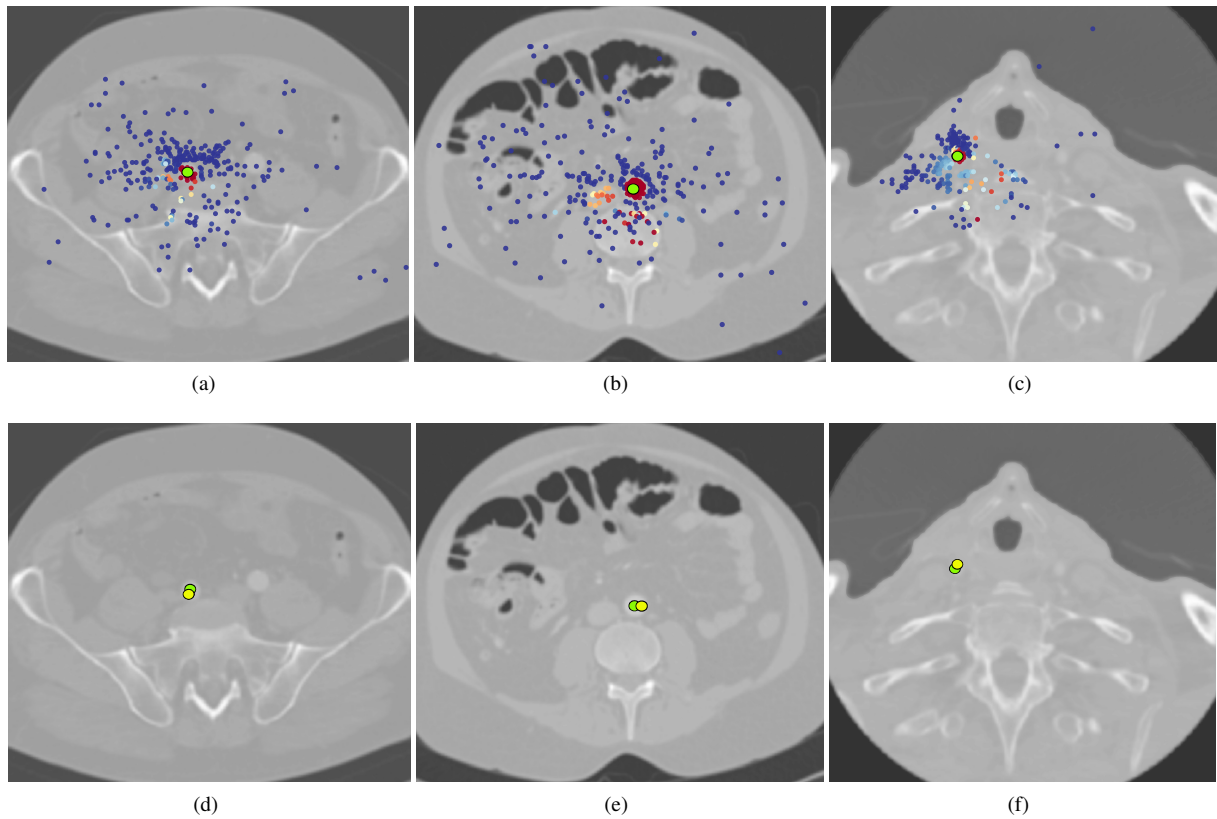

(d)　　　　　　　　　　　(e)　　　　　　　　　　　(f)

Figure 3: *(a)-(c): Regressed candidate position results for RCI, AO and RCC. Ground-truth positions appear as green dots, the remaining dots have colors according to the costs c calculated based on classification probabilities (see Equation 7). Red means low costs and blue high costs. (d)-(f): Slice seed positions computed by MCP for RCI, AO and RCC. Seed positions are visualized by yellow dots and ground-truth points are shown in green.*

3.4. Artery Seed Extraction Performance

After the regressed position candidates were calculated on each slice of $\mathcal{R}^\alpha$, we evaluated the seed detection performance. Here we used the same cross-validation setup as introduced in Section 3.3. In each cross-validation run, Naive Bayes classifiers were trained using 50 artery slice positions sampled from the ground-truth segmentations and 50 non-artery slice positions sampled from outside of the ground-truth segmentation area. The learned classifiers were then applied to the slices of the left-out scan. Slice images showing the regressed candidate positions weighted by the normalized odds ratios (see Equation 7) are visible in Figure 3. The ROI detectors delivered regions completely inside ground-truth and so no further slice selection was performed using the method described in Section 2.4. Thus, the slices of $\tilde{\mathcal{R}}^\alpha$ were identical to the slices of $\mathcal{R}^\alpha$ due to equal lower $\tilde{l}^\alpha = l^\alpha$ and upper bounds $\tilde{u}^\alpha = u^\alpha$. The last step in a cross-validation run was the MCP computation, which returned a final seed position $\mathbf{s}^\alpha_{z_i}$ on each detected artery slice

(see Figure 3). We used the following metrics to measure the slice-based seed detection performance:

1. MCP error (MCPE): The statistics of detected seed position $\mathbf{s}^\alpha_{z_i}$ to the ground-truth slice position $\mathbf{a}^\alpha_{z_i}$ distances.
2. Artery identification rate (AIDR): The ratio of $\mathbf{s}^\alpha_{z_i}$ inside the artery and all detected positions expressed in percentage. We used the artery ground-truth segmentations to decide on positions falling inside the artery.

Both measures are calculated for slices within each artery cross-validation run separately and all runs together (overall performance). The overall AIDR was 94.4 % with an MCPE of 6.52 ± 4.13 mm. All slice-based seed detection performances are shown in Table 2. Our MCPE results are well conform with arterial statistics coming from anatomical studies in the literature. Valecchi et al. [VBG*10] report mean calibers of 16.0 ± 1.1 mm for *AO* and 9.2 ± 1.3 mm for *LCI* and *RCI* based on a study with 250 subjects. Moreover, we achieved high AIDR performances for *LCI*, *RCI*, *AO* and *LCC*. For *AO* there was only 1 dataset out of 9 where seed

positions did not completely follow the artery due to outliers. For *RCI* there was a small deviation in 1 scan out of 5, *LCI* was correct in all 5 cases and *LCC* seeds were affected by outliers in 1 out of 6 datasets. *RCC* arteries showed the lowest performance with 2 problematic cases out of 6. This was due to vein outlier positions next to *RCC* in 2 datasets. Veins have very similar appearance to *RCC* in these datasets, which led to a complete vein detection in the first and to a partial *RCC* and vein detection in the second case. All in all, seeds were detected in all artery slices inside ground-truth segmentations for 26 out of 31 arteries in the 20 scans yielding an overall success rate of 83.8 %.

4. Conclusion and Future Work

In this work we presented a fully-automated artery identification and seed detection approach applied on varying field-of-view CTA scans. Our approach identifies five main arteries using a chain of machine learning steps and includes an anatomical feature capturing the spatial artery-spine relationship. Our results on 20 CTA scans are competitive to recent works and demonstrate its good applicability for the initialization of automated vessel analysis systems. As a future work, we will evaluate our method with a larger set of data and investigate the problematic cases, especially the vein outliers. More than that, we will explore additional features for artery candidate classification such as the cross-sectional diameter in order to increase the robustness of our framework.

Acknowledgements

References

[BBBD10] BECK T., BERNHARDT D., BIERMANN C., DILLMANN R.: Validation and detection of vessel landmarks by using anatomical knowledge. In *SPIE Medical Imaging* (2010), pp. 76234I–76234I. 2

[BFH07] BISHOP Y. M., FIENBERG S. E., HOLLAND P. W.: *Discrete multivariate analysis: theory and practice*. Springer, 2007. doi:10.1007/978-0-387-72806-3. 4

[BGG*12] BROZIO M., GORBUNOVA V., GODENSCHWAGER C., BECK T., BERNHARDT D.: Fast automatic algorithm for bifurcation detection in vascular CTA scans. In *SPIE Medical Imaging* (2012), vol. 8314, pp. 83142U–1. 2

[CGK*11] CAVALLARO A., GRAF F., KRIEGEL H.-P., SCHUBERT M., THOMA M.: Region of interest queries in CT scans. In *Advances in Spatial and Temporal Databases*, vol. 6849 of *LNCS*. Springer, 2011, pp. 56–73. 3

[DT05] DALAL N., TRIGGS B.: Histograms of oriented gradients for human detection. In *IEEE Conference on CVPR* (2005), vol. 1, pp. 886–893 vol. 1. 3, 5

[EGK*10] EMRICH T., GRAF F., KRIEGEL H.-P., SCHUBERT M., THOMA M., CAVALLARO A.: CT slice localization via instance-based regression. In *SPIE Medical Imaging* (2010), vol. 7623, pp. 762320–762320–12. 3

[FHR06] FLEISCHMANN D., HALLETT R. L., RUBIN G. D.: CT angiography of peripheral arterial disease. *Journal of Vascular and Interventional Radiology 17*, 1 (2006), 3–26. 1

[GKS*11] GRAF F., KRIEGEL H.-P., SCHUBERT M., PÖLSTERL S., CAVALLARO A.: 2D image registration in CT images using radial image descriptors. In *MICCAI 2011*, vol. 6892 of *LNCS*. Springer, 2011, pp. 607–614. 3, 5

[GYD*14] GENG C., YANG J., DAI Y., LIU Z., DONG Y.: Spherical operator classification for coronary artery extraction. *Bio-medical materials and engineering 24*, 6 (2014), 3251–3258. doi:10.3233/bme-141147. 1

[HMB15] HLADŮVKA J., MAJOR D., BÜHLER K.: Bone profiles: Simple, fast, and reliable spine localization in CT scans. In *Recent Advances in Computational Methods and Clinical Applications for Spine Imaging*, vol. 20 of *LNCV&B*. Springer, 2015, pp. 173–184. 4

[LAU*06] LELL M. M., ANDERS K., UDER M., KLOTZ E., DITT H., VEGA-HIGUERA F., BOSKAMP T., BAUTZ W. A., TOMANDL B. F.: New Techniques in CT Angiography. *RadioGraphics 26*, suppl_1 (2006), S45–S62. PMID: 17050518. 1

[LKZ14] LOOTUS M., KADIR T., ZISSERMAN A.: Vertebrae detection and labelling in lumbar MR images. In *Computational Methods and Clinical Applications for Spine Imaging*, vol. 17 of *LNCV&B*. Springer, 2014, pp. 219–230. 3

[LL] LEE S.-H., LEE S.: Adaptive kalman snake for semiautonomous 3D vessel tracking. *Computer Methods and Programs in Biomedicine*. In Press. doi:10.1016/j.cmpb.2015.06.008. 1

[ML14] MUJA M., LOWE D.: Scalable nearest neighbor algorithms for high dimensional data. *IEEE Transactions on PAMI 36*, 11 (2014), 2227–2240. 3, 5

[MNBA14] MARQUEZ-NEILA P., BAUMELA L., ALVAREZ L.: A morphological approach to curvature-based evolution of curves and surfaces. *IEEE Transactions on PAMI 36*, 1 (2014), 2–17. 3

[SMH*05] SANDERSE M., MARQUERING H., HENDRIKS E., VAN DER LUGT A., REIBER J.: Automatic initialization algorithm for carotid artery segmentation in CTA images. In *MICCAI 2005*, vol. 3750 of *LNCS*. Springer, 2005, pp. 846–853. 2

[TvWH*13] TANG H., VAN WALSUM T., HAMEETEMAN R., SHAHZAD R., VAN VLIET L. J., NIESSEN W. J.: Lumen segmentation and stenosis quantification of atherosclerotic carotid arteries in CTA utilizing a centerline intensity prior. *Medical physics 40*, 5 (2013), 051721. doi:10.1118/1.4802751. 1

[VBG*10] VALECCHI D., BACCI D., GULISANO M., SGAMBATI E., SIBILIO M., LIPOMA M., MACCHI C.: Assessment of internal diameters of abdominal and femoral blood vessels in 250 living subjects using Color Doppler ultrasonography. *Italian Journal of Anatomy and Embryology 115*, 3 (2010), 180–184. 6

[Yul12] YULE G. U.: On the methods of measuring association between two attributes. *Journal of the Royal Statistical Society 75*, 6 (1912), pp. 579–652. 4

[ZCG14] ZHENG M., CARR J., GE Y.: Automatic aorta detection in non-contrast 3D cardiac CT images using bayesian tracking method. In *Medical Computer Vision. Large Data in Medical Imaging*, vol. 8331 of *LNCS*. Springer, 2014, pp. 130–137. 2